

**Continuous mapping of distributed convection flow
data surrounding auroral arcs to drive 3D simulations**

J. van Irsel¹, K. A. Lynch¹, A. C. Mule¹, M. Zettergren²

¹Department of Physics and Astronomy, Dartmouth College, Hanover, NH, 03755 USA

²Physical Sciences Department, Embry-Riddle Aeronautical University, Daytona Beach, FL, 32114 USA

Key Points:

- Understanding current closure in auroral arc systems requires a fully 3D perspective
- The topside mapping of distributed plasma flow data surrounding auroral arcs should be done anisotropically using auroral imagery
- We provide three methods for developing ionospheric convection flow maps from limited flow data tracks in conjunction with auroral imagery

Version of March 11, 2024

14 **Abstract**

15 Enter your Abstract here

16 **Plain Language Summary**

17 The aurora, or northern and southern lights, are embedded within a complicated
 18 system of interacting electric fields, magnetic fields, and charged particles, the more en-
 19 ergetic of which produce the lights themselves by exciting the neutral atmosphere. This
 20 brings about a 3D electric current system. These currents enter and exit the atmosphere
 21 along the Earth's magnetic field lines, and can only close their circuit between altitudes
 22 of 80 and 150 km. Since auroral arcs often have sheet-like morphologies, this current clo-
 23 sure has been studied extensively in 2D (altitude-latitude), yet not nearly as much in
 24 3D, including variations along the arcs. This paper outlines the importance of simulat-
 25 ing auroral arc systems in 3D and thus the need for generating continuous topside bound-
 26 ary conditions for these simulations. This is difficult as the available data products are
 27 limited. This paper provides three methods of creating these boundary conditions us-
 28 ing multi-color, all-sky auroral imagery in conjunction with approximately across-arc plasma
 29 flow data tracks.

30 **1 Introduction**

31 **1.1 Motivation**

32 Measurements of auroral arc systems are often sparse, heterogeneous, and distributed,
 33 yet ionospheric simulations generally require continuous topside boundary conditions.
 34 Moreover, ionospheric plasma data commonly provide no more than one or perhaps two
 35 sets of dense across-arc data tracks leaving little to no information on along-arc morpholo-
 36 gies. Fortunately, information about these morphologies is something that all-sky im-
 37 agery can provide.

38 This paper provides three methods for creating continuous, topside F-region, elec-
 39 trostatic plasma convection maps from distributed optical data provided by all-sky, multi-
 40 spectral imagery combined with plasma flow data tracks provided by spacecraft, sound-
 41 ing rockets and/or radar measurements. These methodologies focus on typical sheet-like
 42 discrete auroral arc structures with high across- to along-arc gradient ratios. Further-
 43 more, this paper shows the use of these boundary conditions in driving and assessing 3D
 44 auroral ionospheric simulations.

45 The understanding of auroral arc scale science plays an important role in interpret-
 46 ing magnetosphere-ionosphere (MI) coupling, the ionospheric end of which itself involves
 47 ongoing system science studies (Wolf, 1975; Seyler, 1990; Cowley, 2000; Lotko, 2004; Fu-
 48 jii et al., 2011, 2012; Marghitu, 2012; Khazanov et al., 2018; Clayton et al., 2019, 2021;
 49 Yano & Ebihara, 2021; Lynch et al., 2022; Enengl et al., 2023; Wang et al., 2024). MI
 50 coupling studies near auroral arcs demand self-consistent, topside maps of field-aligned
 51 current (FAC) and convection plasma flow consistent with a 3D ionospheric conductiv-
 52 ity volume created by charged particle, auroral precipitation. The auroral ionosphere plays
 53 a non-passive role in this coupling. At high latitudes, the height-integrated topside re-
 54 lation between quasi-static convective flow, FAC, and conductances is (Kelley, 2009, Eq.
 55 8.15):

$$j_{\parallel}(x, y) = \Sigma_P \nabla_{\perp} \cdot \mathbf{E} + \mathbf{E} \cdot \nabla_{\perp} \Sigma_P + (\mathbf{E} \times \mathbf{b}) \cdot \nabla_{\perp} \Sigma_H, \quad (1)$$

56 where j_{\parallel} is the topside map of FAC orthogonal to the local magnetic field, $\Sigma_{P,H}$ are the
 57 height-integrated Pedersen and Hall conductivities, i.e. conductances, \mathbf{E} is the ionospheric
 58 electric field, and $\mathbf{b} = \mathbf{B}/B$ is the magnetic field direction. This explains, in the ab-
 59 sence of induction, how magnetospheric currents and convection patterns couple to the

60 ionosphere given height-integrated conductivity maps using the ionospheric Ohm's law
 61 and current continuity. Integrating out altitudinal effects, however, can hide significant
 62 intuitions to be gained regarding auroral arc systems. Finite, altitude dependent recom-
 63 bination times together with plasma transport can produce 3D electron density struc-
 64 tures providing an auroral precipitation hysteresis in conductance maps. Moreover, the
 65 3D conductivity volume is highly sensitive to auroral precipitation by means of impact
 66 ionization, as the precipitation energy spectra spectra determine ionization rate profiles
 67 that are altitude dependent (Fang et al., 2008, 2010). Altitudinal effects aside, the third
 68 term in Eq. (1) is typically also ignored in sheet-like assumptions, or in some cases where
 69 the ionosphere is modelled as a slab of constant conductance, the second term is ignored
 70 as well. This is why, for proper understanding of MI coupling, it is important to study
 71 the full 3D picture of auroral system science when looking at FAC closure influenced by
 72 auroral precipitation that is both geophysical and self-consistent with plasma convec-
 73 tion. Hence, we need ionospheric simulations that look at the full, 3D current continu-
 74 ity equation, an engagement that requires continuous topside input driver maps.

75 As an important reminder, both Eq. (1) and topics discussed in this paper deal with
 76 self-consistency, not causal relationships, when finding solutions to auroral current con-
 77 tinuity. Hypothesis can be made on causality through intuition, but cannot be proven
 78 within the framework outlined in this paper.

79 1.2 Background

80 Nicolls et al. (2014) undertake the mapping (or "imaging") of electric field distri-
 81 butions using line-of-sight (LOS) plasma flow measurements from a single, multibeam
 82 incoherent scatter radar (ISR). They outline a regularized least-squares fitting algorithm
 83 which takes direct LOS flow measurements, along with their measurement error, and pro-
 84 duces an electric potential map. This is a difficult feat in that a single LOS measure-
 85 ment only carries information on one component of the electric field; multistatic beams
 86 are required to discover information about the full vector field without regularization as-
 87 sumptions. Part of their regularization minimizes the mean squared curvature of the po-
 88 tential field (with an adjustable tailoring parameter) which results in the smoothest pos-
 89 sible solutions and minimizes gradients isotropically, something not well suited near sheet-
 90 like auroral arcs with zeroth order across-arc conductance gradients.

91 Bristow et al. (2016) approach a similar problem but with multiple ISRs by using
 92 Local Divergence-Free Fitting (LDFF), as opposed to a global divergence-free constraint.
 93 They impose the local constraint of divergence-free plasma convection and treat this in
 94 the same way the recombination of two LOS measurements constraint is treated. This
 95 achieves larger gradients, and in turn higher spatial resolution, but this is still indiscrim-
 96 inate to along- or across-arc directions.

97 Laundal et al. (2022) describe methodology for the Local mapping of polar iono-
 98 spheric electrodynamics (Lompe). This is an assimilative tool that gathers relatively dense,
 99 heterogeneous observational data provided by ground/space magnetometers, optical all-
 100 sky observatories, and radars, and performs a regional mapping of the electrodynamics
 101 in the polar ionosphere. They point out that they use Spherical Elementary Current Sys-
 102 tems (SECS) (Amm, 1997) instead of the more global spherical bases used by other as-
 103 similative tools like the Kamide-Richmond-Matsushita (KRM) (Kamide et al., 1981) and
 104 the Assimilative Mapping of Ionospheric Electrodynamics (AMIE) (Richmond & Kamide,
 105 1988) methods, which allows more flexibility when it comes to spatial scales. Again, how-
 106 ever, Lompe is still indiscriminate to gradient directions at the time of writing.

107 In order to address the zeroth order effects of strong and anisotropic conductiv-
 108 ity gradients in the vicinity of auroral arcs, this paper presents, first, a formalization of
 109 techniques developed during the phase A Concept Study Report (CSR) for the Auro-
 110 ral Reconstruction CubeSwarm (ARCS) mission proposal (Lynch et al., 2024; Erland-

son et al., 2024) and second, a continuation of techniques developed by Clayton et al. (2019, 2021) with multiple improvements. We provide methodologies for the continuous mapping of plasma flow data tracks which focus on auroral physical and gradient scale lengths, and discrete sheet-like morphologies, and show how these topside maps can be used as boundary conditions for 3D ionospheric simulations.

116 1.3 Outline.

117 Section 2 describes the reconstruction, replication, and weighted replication methodology
 118 along with example usages of each one. Section 3 outlines and compares two 3D
 119 auroral multi-fluid simulations driven by the plasma flow maps derived by the replica-
 120 tion method in Section 2.2. In section 4 we discuss our results and provide cautionary
 121 remarks, and in Section 5 we conclude this work and outline how we intend to use these
 122 tools in the future.

123 2 Methodologies

124 We outline three methods for developing continuous topside ionospheric plasma flow
 125 maps from limited remote sensed or in situ flow data tracks collected in conjunction with
 126 auroral imagery. Section 2.1 outlines the first methodology, coined “reconstruction”, which
 127 stems from the science section in the ARCS CSR (Lynch et al., 2024). This report pro-
 128 poses an arrayed, localized swarm of spacecraft spanning both multiple latitudes *and* lon-
 129 gitudes, i.e. a “CubeSwarm”. The reconstruction method prioritizes accurate flow rep-
 130 resentation interior to the swarm array and builds the flow map using a set of electric
 131 potential ridges, ensuring electrostatic flow. These ridges follow some definition of a sin-
 132 gle auroral arc boundary determined using morphological features of all-sky, multi-spectral
 133 imagery or, in some cases, maps of FAC from the swarm itself. The left column of Fig-
 134 ure 1 outlines the context of the Observing System Simulation Experiment (OSSE) used
 135 in Lynch et al. (2024) to demonstrate the reconstruction technique. This OSSE is inter-
 136 polated with a virtual spacecraft swarm to provide multi-point, hypothesized in situ plasma
 137 flow data.

138 The second method, “replication”, outlined in Section 2.2, stems from similar method-
 139 ology outlined by Clayton et al. (2019, 2021) who use data from the Isinglass sounding
 140 rocket campaign in conjunction with imagery from the UAF Geophysical Institute’s Poker
 141 Flat Digital All-Sky Camera (DASC) [dasc data ref](#). This method makes use of plasma
 142 flow data from a single auroral arc crossing, whether from a sounding rocket (Clayton
 143 et al., 2019, 2021), spacecraft (Archer et al., 2017), or mesoscale radar (Kaepller et al.,
 144 2023). Here, the data are replicated, scaled, and rotated in accordance with *two* auro-
 145 ral arc boundaries, again, determined through all-sky imagery features. The right col-
 146 umn of Figure 1 shows the context of the simulation used to demonstrate the replica-
 147 tion technique.

148 The third method, a permutation of the second named “weighted replication”, is
 149 outlined in Section 2.3 and uses two (or more) tracks in conjunction with all-sky imagery.
 150 This method repeats part of the replication methodology for each track and then per-
 151 forms a weighted averaging on the interpolated flow maps (prior to enforcing electrostat-
 152 ics) with the weighting being based on the geometric distances to either track.

153 In all three methods, one of the main difficulties in creating a continuous plasma
 154 flow map lies in the constraint that it is divergence-free, i.e. electrostatic (Ruohoniemi
 155 et al., 1989; Nicolls et al., 2014). Vector fitting algorithms exist which handle this con-
 156 straint, but will often provide large vortices to act as sources/sinks, replacing points of
 157 divergence/convergence, and, significantly, are not designed to be constrained by asso-
 158 ciated information from auroral arc boundaries.

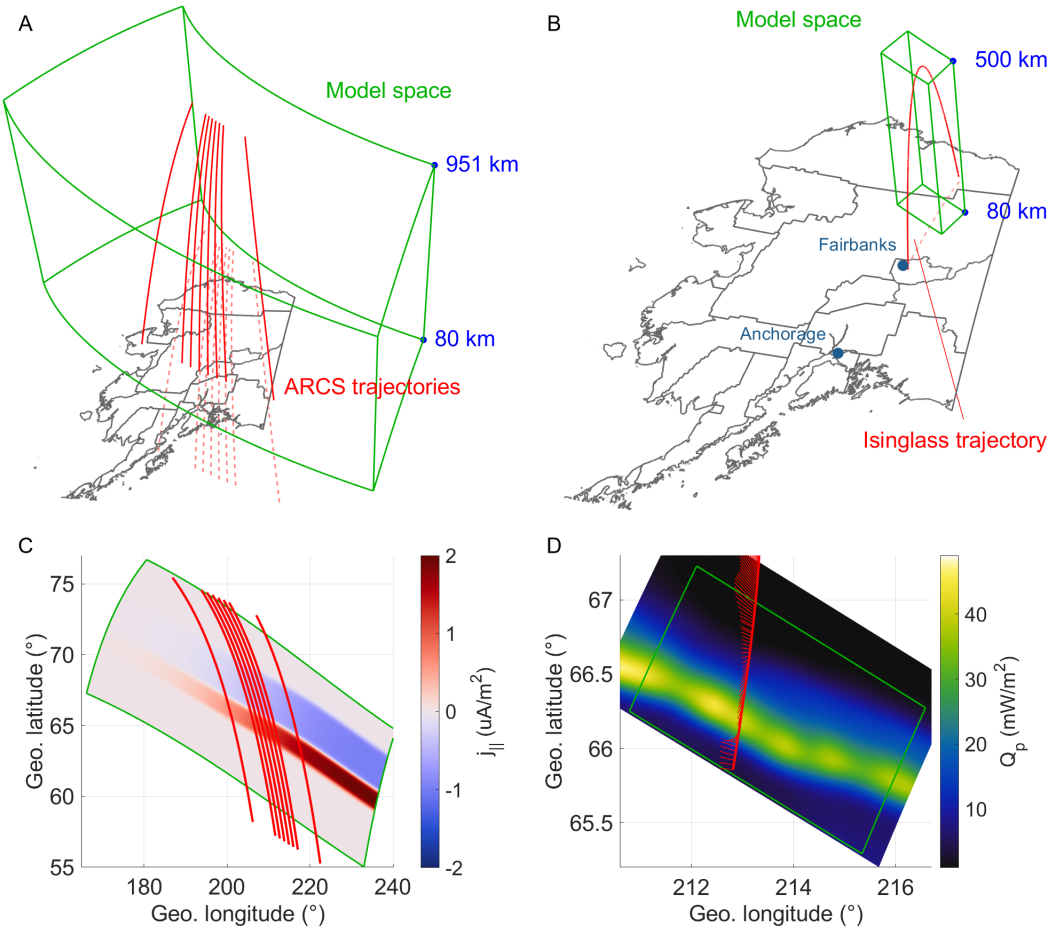


Figure 1. Context relating to the simulations used in demonstrating the reconstruction and replication methods. **A:** The simulation model space (green) and the ARCS trajectories (red) in reference to Alaska. **B:** Same as panel A but with the Isinglass trajectory. **C:** Topside FAC simulation driver map in reference to the model space (green) and ARCS orbits (red). **D:** Total precipitating energy flux (colormap) and plasma flow data (red) in reference to the model space (green outline). Data sources: in-text.

159 **2.1 Reconstruction**

160 This section provides a proof-of-concept reconstruction using an OSSE used by Lynch
 161 et al. (2024) wherein a localized “CubeSwarm” of virtual spacecraft scrape data from a
 162 3D auroral arc simulation as they orbit through (see Figure 1A). The simulation used
 163 in this section is data-inspired, but idealized; it is driven with a topside map of a sin-
 164 gle pair of mostly east-west aligned FAC sheets with a slight bend in their profile and
 165 the amplitudes of which fade westward from ± 1 to $0 \mu\text{A}/\text{m}^2$ over the span of the model
 166 space (see Figure 1C). The associated auroral arc precipitation input maps are of a sim-
 167 ilarly shaped arc embedded within the poleward FAC sheet peaking at an energy flux
 168 of $3 \text{ mW}/\text{m}^2$ and characteristic energy of 3 keV with gradient scale lengths of 40 km.

169 **2.1.1 Reconstruction algorithm**

170 With intuition as to what the form of the electric potential map is, and to avoid
 171 large plasma flow vortices, we construct the potential map out of a sum of a user-defined
 172 number, N_k , of east-north dependent pseudo-basis functions, ϕ_k , each governed by a set
 173 of parameters. The functional form of each of them is an inclined Gaussian ridge, i.e.
 174 a Gaussian profile northward that extrudes east- and westward with a constant sloped
 175 amplitude while following the curved boundary of the arc. *This is done to find electric*
 176 *potential solutions that prioritize across-arc gradients while remaining relatively unstruc-*
 177 *tured along the arc.* The $\mathbf{E} \times \mathbf{B}$ plasma flow derived from this potential field is then com-
 178 pared against the virtual plasma flow data and their mean square differences are then
 179 minimized over the parameter space.

180 The arc boundary is determined using standard Sobel edge detection (Sobel, 2014).
 181 Given the idealistic nature of the OSSE used in demonstrating this method, this suffices,
 182 but we caution the reader regarding the complexities of determining less idealized arc
 183 boundaries. In any case, after determining an appropriate set of boundary points, they
 184 are least-squares fit against the following functional form:

$$b(x; \bar{A}) = \sum_{j=1}^{N_j} \left[A_{j1} + A_{j2} \tanh\left(\frac{x - A_{j3}}{A_{j4}}\right) \right], \quad (2)$$

185 with \bar{A} being the $N_j \times 4$ fitting boundary parameter matrix, N_j the user-defined num-
 186 ber of summation terms, and x the linear magnetic east coordinate. Throughout this manuscript,
 187 the coordinates x , y , and z refer to linear magnetic east, north, and up, and we oper-
 188 ate in the northern hemisphere. The reason for the choice of summing hyperbolic tan-
 189 gents lies in the tendency of auroral arcs to be aligned magnetic east-west and to be rel-
 190 atively unstructured in this direction.

191 With this, we define our pseudo-basis potential ridge as

$$\phi_k(\mathbf{r}; \bar{P}, \bar{A}) = (P_{k1}x + P_{k2}) \exp\left[-\frac{(y - P_{k3} - b(x; \bar{A}))^2}{P_{k4}^2}\right], \quad (3)$$

192 where \bar{P} is the $N_k \times 4$ potential parameter matrix, giving a total potential field of

$$\phi(\mathbf{r}; \bar{P}, \bar{A}) = \sum_{k=1}^{N_k} \phi_k(\mathbf{r}; \bar{P}, \bar{A}). \quad (4)$$

193 Prior work by(Clayton et al., 2021, Appx. A) aimed to instead warp the flow field via
 194 a coordinate transformation to along/across-arc coordinates, similar to those used by Marghitu
 195 (2012), but we have found the solution used here to be both simpler to implement and
 196 faster in this context.

197 The plasma flow data from the virtual spacecraft provide the vectors $\mathbf{v}_i = (v_{xi}, v_{yi})$
 198 at positions $\mathbf{r}_i = (x_i, y_i)$ with i being the sample number. Generally, this flow data would

require some mindful Gaussian smoothing, but more on this in Section 4.2. With this, the electric field components to be compared against the plasma flow data are

$$\begin{aligned} E'_x(\mathbf{r}_i; \bar{P}, \bar{A}) &= -\frac{\partial}{\partial x}\phi(\mathbf{r}; \bar{P}, \bar{A})\Big|_{\mathbf{r}_i} \\ &= -\sum_{k=1}^{N_k} \left[P_{k1} + \frac{2\gamma(\mathbf{r}_i; \bar{P}, \bar{A})}{P_{k4}^2} (P_{k1}x_i + P_{k2}) \frac{\partial b}{\partial x}\Big|_{x_i} \right] \exp\left[-\frac{\gamma(\mathbf{r}_i; \bar{P}, \bar{A})^2}{P_{k4}^2}\right] \end{aligned} \quad (5)$$

$$\begin{aligned} E'_y(\mathbf{r}_i; \bar{P}, \bar{A}) &= -\frac{\partial}{\partial y}\phi(\mathbf{r}; \bar{P}, \bar{A})\Big|_{\mathbf{r}_i} \\ &= \sum_{k=1}^{N_k} \frac{2\gamma(\mathbf{r}_i; \bar{P}, \bar{A})}{P_{k4}^2} (P_{k1}x_i + P_{k2}) \exp\left[-\frac{\gamma(\mathbf{r}_i; \bar{P}, \bar{A})^2}{P_{k4}^2}\right], \end{aligned} \quad (6)$$

with $\gamma(\mathbf{r}; \bar{P}, \bar{A}) = y - P_{k3} - b(x; \bar{A})$ and

$$\frac{\partial b}{\partial x} = \sum_{j=1}^{N_j} \frac{A_{j2}}{A_{j4}} \operatorname{sech}^2\left(\frac{x - A_{j3}}{A_{j4}}\right). \quad (7)$$

From here, with $\mathbf{B} = -B\hat{z}$, we rotate the electric field providing (non-optimized) plasma flow:

$$\mathbf{v}'(\mathbf{r}; \bar{P}, \bar{A}) = (v'_x, v'_y, 0) = \frac{\mathbf{E}' \times \mathbf{B}}{B^2} = \frac{1}{B} (-E'_y, E'_x, 0). \quad (8)$$

This reduces the problem to finding the parameter matrix, \bar{P}^0 , which solves

$$\min_{\bar{P}} \sum_i [(v'_x(\mathbf{r}_i; \bar{P}, \bar{A}^0), v'_y(\mathbf{r}_i; \bar{P}, \bar{A}^0)) - (v_{xi}, v_{yi})]^2, \quad (9)$$

where \bar{A}^0 is the best fitting boundary parameter matrix, such that the continuous plasma flow map is given by

$$\mathbf{v}_c(\mathbf{r}) = \mathbf{v}'(\mathbf{r}; \bar{P}^0, \bar{A}^0) \quad (10)$$

and subsequently the continuous potential map used to drive ionospheric models is

$$\phi_c(\mathbf{r}) = \phi(\mathbf{r}; \bar{P}^0, \bar{A}^0). \quad (11)$$

By using the potential ridges, we prioritize solutions for ϕ_c that have sheet-like morphology in contrast to what has been done before (Kamide et al., 1981; Amm, 1997; Nicolls et al., 2014; Bristow et al., 2016; Laundal et al., 2022). This maintains strong potential gradients normal to the arc boundary.

2.1.2 Reconstruction example

Figure 2 shows an example use of the reconstruction algorithm. This example was developed for the proposed ARCS mission (Lynch et al., 2024) to verify the ability of plasma flow reconstruction given a local grouping of spacecraft. The virtual orbits are arranged densely to provide maps of along- and across-arc gradients.

The black dashed lines are the imagery derived boundary, b , and the bag of plasma flow vectors, \mathbf{v}_i , is overlaid in red. The reconstructed electric potential, ϕ_c , and reconstructed flow, \mathbf{v}_c , match well within the spacecraft region (gray outline in Fig. 2C, F) as per design. The maximum absolute flow difference in this region is 47 m/s eastward and 28 m/s northward with averages of 5(12) and 5(8) m/s. Outside the region, however, the error quickly ramps up given the the under-regulated potential ridge parameters, \bar{P} .

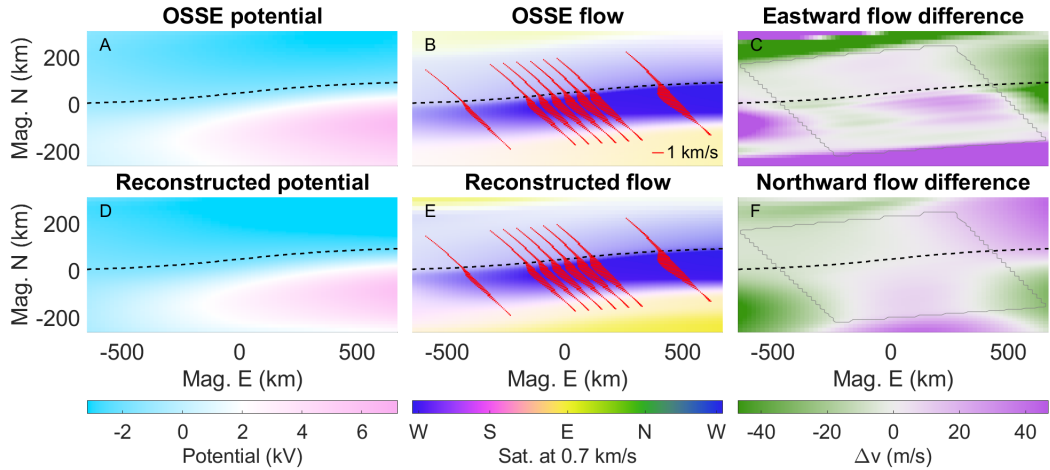


Figure 2. Example of a plasma flow field reconstruction. **A:** The electric potential map used to drive the OSSE with the boundary, b , overlaid. **B:** The resulting flow field with the virtual flow data points (red), \mathbf{v}_i , interpolated from it. The color representation of flow has the direction depicted by hue and the intensity by the color saturation. **D, E:** The reconstructed electric potential, ϕ_c , and flow, \mathbf{v}_c . **C, F:** The difference between the reconstructed and OSSE east- and northward flow with the gray outline being the region of interest.

224 2.1.3 Possible improvements

225 Proper regularization on the potential ridges, ϕ_k , can be used to stretch the well-
 226 fitted region as presently the goodness-of-fit rapidly decreases when moving away from
 227 the spacecraft. The electric field resulting from a single ridge i.e. Eqs. (5-6), far from the
 228 fitting region is

$$\lim_{\mathbf{r} \rightarrow \infty} E_{xk}(\mathbf{r}; \bar{P}, \bar{A}) = -P_{k1} \exp \left[-\frac{(y - P_{k3} - b_{\pm\infty})^2}{P_{k4}^2} \right] \quad (12)$$

$$\lim_{\mathbf{r} \rightarrow \infty} E_{yk}(\mathbf{r}; \bar{P}, \bar{A}) = \frac{2}{P_{k4}^2} (P_{k1}x + P_{k2})(y - P_{k3} - b_{\pm\infty}) \exp \left[-\frac{(y - P_{k3} - b_{\pm\infty})^2}{P_{k4}^2} \right], \quad (13)$$

230 where $b_{\pm\infty} = \sum_j (A_{j1} \pm A_{j2})$ and $\partial b / \partial x (x \rightarrow \pm\infty) \rightarrow 0$. Clearly, E_{xk} remains finite,
 231 but E_{yk} diverges as $|y| < \infty \wedge x \rightarrow \infty$. Granted we work within the bounds of the
 232 model space, but slowing down this divergence would aid in regularization and provide
 233 smoother solutions and, in actuality, models often require a good amount of buffer sur-
 234 rounding the region of interest into which the flow map needs to extrapolate. Lastly, in-
 235 incorporating weighted fitting would provide error estimates for reconstructions from real
 236 data as opposed to an OSSE, e.g. weights of $w_i = 1/\sigma_i^2$ with σ_i being instrument er-
 237 ror assuming a diagonal measurement covariance matrix.

238 2.2 Replication

239 The second method of developing continuous topside plasma flow maps uses indi-
 240 vidual approximately across-arc tracks of plasma flow data in conjunction with all-sky,
 241 multi-spectral imagery. In this method, data points are replicated in the along-arc di-
 242 rection using direct and indirect information from the imagery. Primary *and* secondary
 243 boundaries are determined along which the data track is translated, scaled, and the flow
 244 data are rotated to be tangent with the primary boundary. The example here uses data
 245 set “c5” from Clayton et al. (2021).

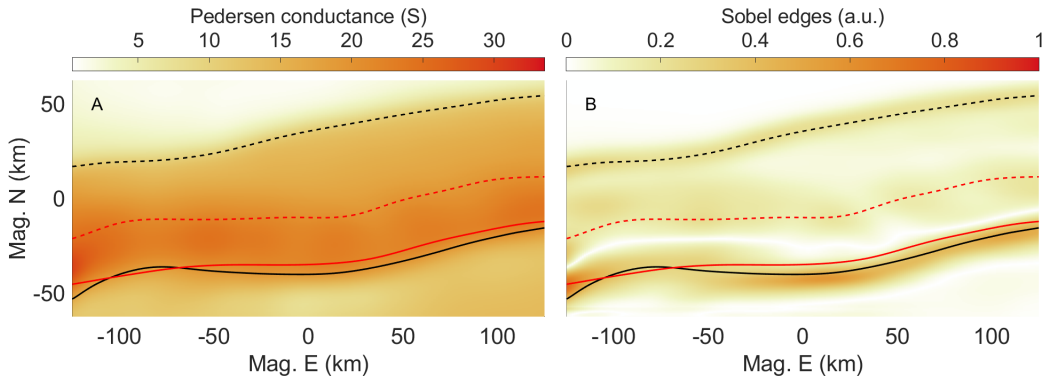


Figure 3. Primary (solid) and secondary (dashed) boundaries using Pedersen conductance and contour lines at 19.1 S and 10.5 S (black). In red are the boundaries determined using the energy flux (not shown) with the steepest gradient method, as is done by Clayton et al. (2019, 2021). **A:** Pedersen conductance determined via Eq. (14). **B:** Magnetic northward Sobel convolution of the Pedersen conductance. Both sets of boundaries have an approximate smoothing window of 15 km.

246 2.2.1 Arc boundary definitions

Determining the arc boundaries from multi-spectral imagery data first requires an inversion (Grubbs II, Michell, Samara, Hampton, Hecht, et al., 2018; Grubbs II, Michell, Samara, Hampton, & Jahn, 2018) to a map of total energy flux, Q_p , and characteristic energy, E_p , of the precipitating electrons. From these a proxy for the Pedersen conductance is made which, at the time of writing, is done using Eq. (3) by Robinson et al. (1987):

$$\Sigma_P(x, y) = \frac{40(E_p(x, y)/\text{keV})}{16 + (E_p(x, y)/\text{keV})^2} \left(Q_p(x, y)/\text{mW/m}^2 \right)^{1/2}. \quad (14)$$

The reader is cautioned, however, to use multi- and/or two-stream transport models (similar to how Q_p and E_p are determined), such as the GLobal airglOW (GLOW) model (Solomon, 2017), or look-up tables generated by such models, to determine a more accurate Pedersen conductance.

With this, the primary and secondary arc boundaries are established in one of two ways using *either* the total energy flux *or* Pedersen conductance (for a total of four options): 1) finding the magnetic latitude of the first two most prominent edges at each magnetic longitude using Sobel edge detection (Sobel, 2014) in the magnetic northward direction, or 2) following a contour line at two isovalues which can be chosen directly, or determined at the locations of the central two most prominent edges along the track. In all cases, the boundaries are minimally Gaussian smoothed. Figure 3 shows the Pedersen conductance and its magnetic northward Sobel convolution along with the primary and secondary boundaries determined using method 2 with Pedersen conductance and method 1 with total energy flux. In the remainder of this paper, we use boundaries determined using Pedersen conductance contour lines.

267 2.2.2 Flow data replication

First, the plasma flow data track is Gaussian smoothed (more on this in Section 4.2) and, prior to doing any replication, we split the flow field into two components: 1)

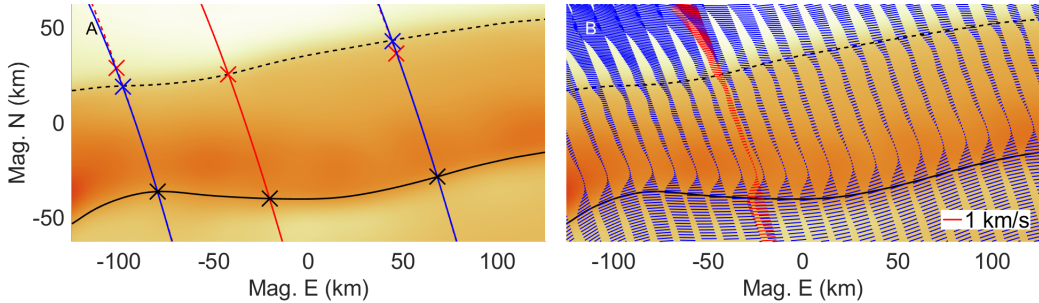


Figure 4. In situ trajectory flow data replication overlaid on the same conductance map from Figure 3A. **A:** Two example replications (blue) of the original trajectory (red) along the primary arc boundary (solid black). The black crosses have the same flow data. The red/blue crosses indicate flow data before/after scaling to meet up with the secondary arc boundary (dashed black). **B:** A low density replication (blue) along with the original, smoothed flow data (red). Data source: in-text.

the background flow treated as a constant, large-scale, global disturbance, and 2) the small-scale disturbances imposed by the arc itself:

$$\mathbf{v}(\mathbf{r}) = \mathbf{v}_{\text{arc}}(\mathbf{r}) + \mathbf{v}_{\text{bg}}. \quad (15)$$

Throughout the remainder of Section 2, this background flow is put aside and is only added back when performing 3D simulations (see Section 3.2). In absence of background flow, the most basic model of an auroral arc is composed of only across-arc flow shear, i.e. electric field shocks (Marghitu, 2012). Thus, we define the background flow such that, once removed, the flow at the intersection of the track and the primary boundary is tangent to that boundary. Furthermore, this simplistic model has the arc defined as a band of enhanced conductance in which we expect the electric field to quench. Thus, it makes sense to replicate these data along the arc boundaries, while remaining tangent to it, and scaling such that the shorted out electric fields remain inside the area of enhanced conductance. This leads to the following plasma flow data track replication algorithm:

1. The original track is translated by some amount following the primary arc boundary such that the original and replicated flow data are equal at the primary boundary-track intersections.
2. The replicated track is scaled in the along-track direction such that the original and replicated flow data are equal at the secondary boundary-track intersections.
3. The flow data of the replicated track is rotated by a constant angle per track such that it remains to be tangent to the primary arc boundary.
4. This replication is repeated for multiple translations along the arc until the top-side boundary space is filled with a replication rate higher than the eastward Nyquist spacing.

Figure 4 illustrates these steps given the boundaries of Figure 3. The left panel shows two examples of how replications of the original trajectory are translated and scaled. The western replication example is scaled down to have the data at the red cross meet the secondary boundary, while the eastern replication is scaled up to do the same. The right panel shows the replication, but done only for a few instances for illustration purposes. This also shows the rotated flow vectors keeping tangent with the primary boundary.

299 **2.2.3 Enforcing electrostatic flow**

300 This replicated flow field is not generally divergence-free; its electric field can have
 301 a curl which must be removed. The replicated flow data are interpolated onto the model
 302 grid (again, more on this in Section 4.2). This section outlines three choices of fitting
 303 an electric potential map to this interpolated flow field, $\mathbf{v}_{\text{arc}} = \mathbf{E}_{\text{arc}} \times \mathbf{B} / B^2$, where \mathbf{B}
 304 is the magnetic field from Eq. (8) and \mathbf{E}_{arc} is the arc disturbed ionospheric electric field
 305 perpendicular to \mathbf{B} . The interpolated flow fields' associated electric field reads as follows:

$$\mathbf{E}_{\text{arc}}(\mathbf{r}) = -\mathbf{v}_{\text{arc}}(\mathbf{r}) \times \mathbf{B} = \mathbf{E}_I(\mathbf{r}) + \mathbf{E}_S(\mathbf{r}) = -\nabla\phi_c(\mathbf{r}) + \nabla \times \mathbf{A}(\mathbf{r}), \quad (16)$$

306 where ϕ_c is the electric potential map we're looking for and \mathbf{A} is the magnetic vector po-
 307 tential. We want to remove the non-electrostatic part, i.e. find the irrotational electric
 308 field, \mathbf{E}_I , and remove the solenoidal field, \mathbf{E}_S , in a way that best agrees with the inter-
 309 polated flow field. Two choices of doing so are as follows:

- 310 1. **Brute force:** Perform a least-squares fitting algorithm (Levenberg–Marquardt
 311 in our case) that directly fits a potential map, ϕ , i.e.

$$\min_{\phi} \|\nabla \times \mathbf{A}(\mathbf{r})\|_2^2 = \min_{\phi} \|\nabla\phi(\mathbf{r}) + \mathbf{E}_{\text{arc}}(\mathbf{r})\|_2^2 = \min_{\phi} \sum_{i,j} \left((\nabla\phi)_{ij} + \mathbf{E}_{\text{arc},ij} \right)^2, \quad (17)$$

312 the solution of which, ϕ_c , is the continuous potential map we want.

- 313 2. **Helmholtz decomposition:** Use the Fourier transform method for Helmholtz
 314 decomposition. Taking the spatial Fourier transform of Eq. (16) gives us

$$\mathbf{G}(\mathbf{k}) = -ikG_{\phi}(\mathbf{k}) + ik \times \mathbf{G}_{\mathbf{A}}(\mathbf{k}), \quad (18)$$

315 where $\mathbf{k} = (k_x, k_y)$ is the wave vector and \mathbf{G} , G_{ϕ} , and $\mathbf{G}_{\mathbf{A}}$ are the Fourier trans-
 316 forms of \mathbf{E}_{arc} , ϕ_c , and \mathbf{A} respectively. Taking the dot product of Eq. (18) with
 317 \mathbf{k} gives us an expression for the Fourier transform of the potential:

$$G_{\phi}(\mathbf{k}) = i \frac{\mathbf{k} \cdot \mathbf{G}(\mathbf{k})}{\|\mathbf{k}\|^2}, \quad (19)$$

318 such that

$$\phi_0(\mathbf{r}) = \mathcal{F}^{-1}\{G_{\phi}(\mathbf{k})\} = \int_{-\infty}^{+\infty} dk_x \int_{-\infty}^{+\infty} dk_y G_{\phi}(\mathbf{k}) e^{i(xk_x + yk_y)}. \quad (20)$$

319 Here we've found the electric potential up to a harmonic function (i.e. gauge in-
 320 variance). The potential map we want is $\phi_c = \phi_0 + f$ where $\nabla^2 f = 0$. One choice
 321 of f has the average electric field remain the same such that

$$f_a(\mathbf{r}) = \langle -\nabla\phi_0(\mathbf{r}) - \mathbf{E}_{\text{arc}}(\mathbf{r}) \rangle \cdot \mathbf{r}. \quad (21)$$

322 A second option for f solves the optimization problem

$$\min_{\bar{F}} \left\| -\nabla(\phi_0(\mathbf{r}) + f_b^m(\mathbf{r}; \bar{F})) - \mathbf{E}_{\text{arc}}(\mathbf{r}) \right\|_2^2 \text{ with } \mathbf{r} \in \mathcal{M}, \quad (22)$$

323 where \bar{F} is an $m \times 2$ parameter matrix, \mathcal{M} is a user defined masking domain sur-
 324 rounding the primary and/or secondary boundary, and original track, and f_b^m is
 325 the most general m order polynomial in x and y that satisfies Laplace's equation:

$$f_b^m(\mathbf{r}; \bar{F}) = \sum_{n=1}^m \sum_{q=0}^{\lfloor n/2 \rfloor} (-1)^q \left[\frac{F_{n1}}{\rho^{n-1}} \binom{n}{2q+1} x^{2q+1} y^{n-2q-1} + \frac{F_{n2}}{\rho^{n-1}} \binom{n}{2q} x^{2q} y^{n-2q} \right], \quad (23)$$

326 where ρ is a regularization parameter balancing higher order terms. To show this
 327 is the most general case, take the complex polynomial of degree m

$$p(z) = \sum_{n=0}^m F_n^* z^n, \text{ where } z^n = (x + iy)^n = \sum_{q'=0}^n \binom{n}{q'} x^{q'} (iy)^{n-q'}, \quad (24)$$

328 and recognize that the homogeneous polynomial z^n is analytic which therefore has
 329 harmonic real and imaginary parts (Ahlfors, 1953). This gives two parameters,
 330 the real and imaginary parts of F_n^* , for each value of n . To show uniqueness, we
 331 recognize that the Laplacian maps homogeneous polynomials of degree n to those
 332 of degree $n-2$, the domain and image of which have dimensions n and $n-2$ re-
 333 spectively. By the rank nullity theorem, this means the dimension of the kernel
 334 of the Laplacian is $n-(n-2) = 2$, so we've found all solutions. An example for
 335 $m = 2$ and $\rho = 10$ gives

$$f_b^3(x, y, \bar{F}) = F_{11}x + F_{12}y + \frac{F_{21}}{10}(x^2 - y^2) + \frac{F_{22}}{10}xy. \quad (25)$$

336 Note that x , y , and q in meters and \bar{F} in V/m has f_b in volts. When solving
 337 for this optimization the initial guess is taken to be $(f_2^m)_0 = f_a$.

338 Along with the interpolated flow field (column 1), examples of the the brute force and
 339 Helmholtz decomposition methods are shown in Figure 5 (columns 2-3). The divergence
 340 panel shows that of the interpolated flow field and indicates the location of rotational
 341 signatures which are interpretable as Alfvénic. Although the brute force method is eas-
 342 iest to justify being the “best” fit, it is also by far the slowest, taking at least several hours
 343 on a clustered machine. The Helmholtz decomposition method, on the other hand, has
 344 the advantage of using the fast Fourier transform method and it compares reasonably
 345 well, even when using the direct harmonic solution, f_a . This is illustrated in Figure 6
 346 which shows the residual between the brute force solution and the potential from Eq. (20)
 347 compared against a masked and unmasked harmonic fit. Clearly, a constant background
 348 electric field match, i.e. a harmonic function that is constant sloped plane, f_a , is a first
 349 order solution in this particular case but this requires further confirmation for other cases.
 350 The masking acts as a binary placeholder for a continuous error based weighting map.
 351 Such an improved map will aid in constraining the potential in the corners of the model
 352 space (see Figure 6C).

353 2.2.4 Replication example

354 Figure 7 shows the replication methodology applied to the “c5” example by Clayton
 355 et al. (2021) (see their Table 1). The top row has the scaling and rotating applied, whereas
 356 the bottom row is done with neither. For the top row, the masked 2-sigma ranges of the
 357 residuals in enforcing electrostatics are ± 106 m/s eastward and ± 142 m/s northward. For
 358 the bottom row, these numbers are ± 84 m/s and ± 101 m/s. More qualitatively, the ap-
 359 plied scaling to the replication results in a co-location of the shorted out electric field
 360 and the auroral precipitation as seen by the Σ_P contour lines in panel A, in compari-
 361 son to panel D. Secondly, the applied rotation provides more streamlined plasma flow,
 362 in the literal sense, as seen by the change from southwest to west to southwest flow in
 363 panel A. In contrast, without rotation the flow remains westward resulting in a chang-
 364 ing angle between the electric field and the conductance gradients. This has physical ef-
 365 fects on auroral current closure (see Eq. (1)).

366 2.3 Weighted replications

367 In the event of a conjunction between auroral imagery and two flow data tracks,
 368 the replication method can simply be repeated up to the interpolation step. Both repli-
 369 cations use the same primary and secondary boundaries as well as the same background

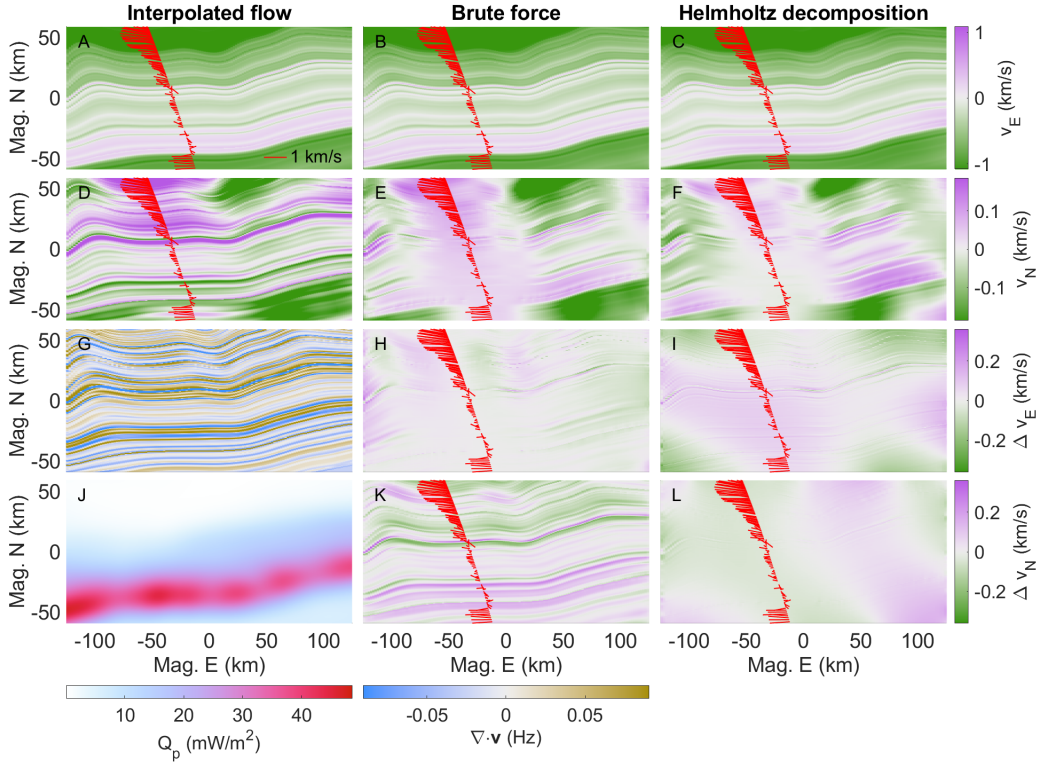


Figure 5. Comparison of methods for determining a potential map from an interpolated flow map, \mathbf{v}_{arc} . In red are the in situ plasma flow data which have no smoothing applied in an effort to stress test these methods. **A-C:** Eastward interpolated, brute force fitted, and Helmholtz decomposed flow. **D-F:** Same but northward. **G:** Divergence of the interpolated flow. **H, K:** Difference in east and northward flow between brute force and interpolated. **I, L:** Difference in east and northward flow between Helmholtz decomposed and brute force. **J:** Total precipitating energy flux (for reference). Data source: in-text.

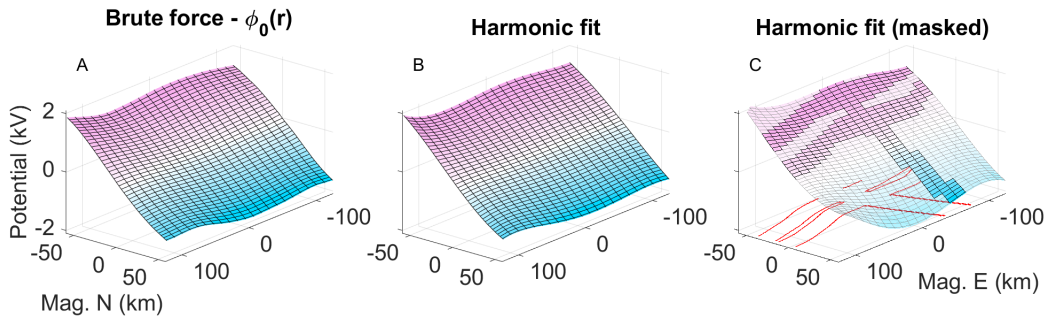


Figure 6. Validity of a harmonic function fit. **A:** Residual potential between brute force fitting and Eq. (20). **B:** Unmasked harmonic function fit from Eq. (23) with $m = 5$ and $q = 10$ m. **C:** Same as panel B but masked with the mask, \mathcal{M} , in red.

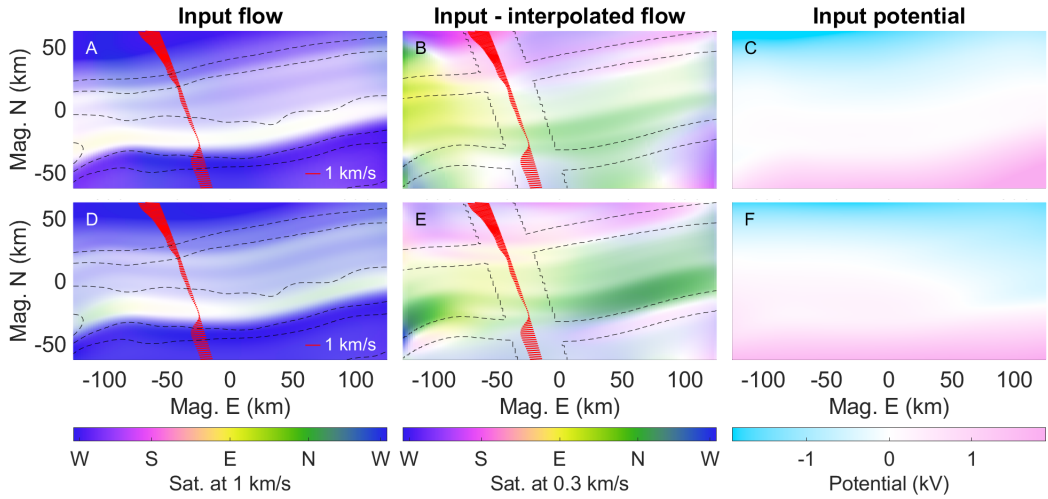


Figure 7. Input flow and potential maps used to drive simulations with (top row) and without (bottom row) replication scaling/rotating. **A, D:** Hue-saturation plots of $-\nabla\phi_c$ with contour lines of Σ_P . **B, E:** Flow error, i.e. $-\nabla\phi_c - \mathbf{v}_{\text{arc}}$, with masking contours where the harmonic function is fit. **C, F:** Input potential maps, ϕ_c . Data source: in-text.

flow, \mathbf{v}_{bg} . This background flow is determined by whichever replication is done first. The flow data smoothing is also performed with approximately equal Gaussian filter physical window widths.

Once both tracks have their replication and subsequent interpolated flow fields, they are weighted averaged with the weighting functions

$$w_A(\mathbf{r}) = \frac{1}{2} \left[1 + \tanh \left(\frac{d_{\min,B}(\mathbf{r}) - d_{\min,A}(\mathbf{r})}{s_w} \right) \right], w_B(\mathbf{r}) = 1 - w_A(\mathbf{r}). \quad (26)$$

Here, $d_{\min,A}$ is a map of the shortest straight-line distances from points \mathbf{r} to track A and similarly for track B . This configuration of weighting allows for two intersecting tracks. The scale length, s_w , will introduce flow gradients and has to be chosen with care. From here we have a new interpolated arc-disturbed plasma flow,

$$\mathbf{v}_{\text{arc}}(\mathbf{r}) = w_A(\mathbf{r})\mathbf{v}_{\text{arc},A}(\mathbf{r}) + w_B(\mathbf{r})\mathbf{v}_{\text{arc},B}(\mathbf{r}), \quad (27)$$

from which the methodology from Section 2.2.3 takes over. This ensures electrostatics, but it should be mentioned that, on top of the divergences still remaining in either track's interpolated field, this weighting function introduces additional divergence of the form

$$(\nabla \cdot \mathbf{v}_{\text{arc}})_w = \nabla w_A(\mathbf{r}) \cdot (\mathbf{v}_{\text{arc},A} - \mathbf{v}_{\text{arc},B}). \quad (28)$$

This weighting function, however, has small northward gradients and the interpolated flows are expected to not vary much eastward, i.e. ∇w_A is approximately orthogonal to $\mathbf{v}_{\text{arc},A} - \mathbf{v}_{\text{arc},B}$ resulting in minimal diverging flow. This ensures that the subsequent Helmholtz decomposition provides an electrostatic solution of the final flow map that doesn't stray far from the interpolated flow map.

For more than two replications the weighting function requires some adjustments, but this is also perfectly possible.

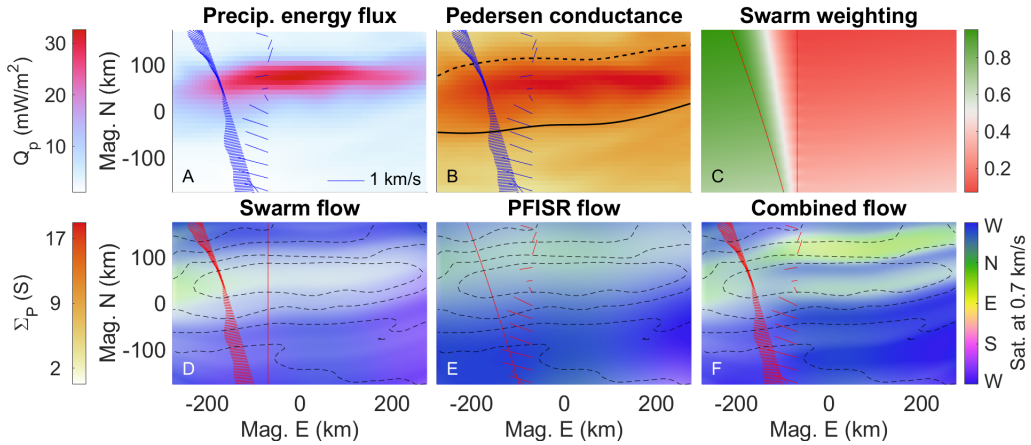


Figure 8. Weighted replication example. **A:** Precipitating total electron energy flux with plasma flow data from Swarm (left trajectory) and PFISR (right track) in blue. **B:** The GLOW derived Pedersen conductance with the primary (solid) and secondary (dashed) boundaries overlaid. **C:** The weighting map, w_A , used for the Swarm data with a scale length of $s_w = 200$ km. **D-F:** Resulting flow maps from using only Swarm data, only PFISR data, and from using both datasets, respectively. Data sources: in-text.

389

2.3.1 Weighted replication example

390
391
392
393
394
395
396
397
398

To illustrate the double replication methodology, a conjunction from the *Swarm-over-Poker-2023* campaign is used (Feb - March 2023, Poker Flat Research Range, AK). This campaign facilitated conjunctions of (among a variety of other data) ion flow data from the Thermal Ion Imagers (Knudsen et al., 2017) on ESA's Swarm mission, convection flow data from AMISR's Poker Flat Incoherent Scatter Radar (PFISR) (Kelly & Heinselman, 2009; Nicolls & Heinselman, 2007; Heinselman & Nicolls, 2008), and multi-spectral, all-sky imagery from the Poker Flat DASC [dasc data ref](#). This campaign has developed a growing collection of heterogeneous auroral observations for the winter months of 2023. Our example uses data from March 19 at 8:23:44 UT (20.5 MLT).

399
400
401
402
403
404
405
406
407
408
409

Figure 8A summarizes this event showing a $Q_p \approx 30$ mW/m² (with $E_p \approx 7$ keV, not shown) auroral arc with some along-arc structure. The left trajectory shows flow data from Swarm B and the right track shows that from PFISR. Panel B also shows the Pedersen conductance (this time inverted using GLOW (Solomon, 2017)) which is used to determine the arc boundaries and panel C shows the the weighting function used for the Swarm data. The bottom row gives the final continuous plasma flow maps when using only the Swarm data, or the PFISR data, or both. The individual reconstructions are dissimilar, but this is to be expected given the along-arc structure. The final combined flow (panel F) before and after enforcing electrostatics have residual 2-sigma standard range of ± 91 m/s eastward and ± 157 m/s northward. [Note about how swarm B data was constructed \(ask Alex\)](#).

410

3 Driving GEMINI using Replication

411

3.1 The GEMINI model

412
413
414

To investigate the effects of continuous topside plasma flow maps in conjunction with auroral precipitation, we use state-of-the-art 3D ionospheric simulations provided by the Geospace Environment Model of Ion-Neutral Interactions (GEMINI) (M. D. Zetter-

415 gren & Semeter, 2012; M. Zettergren & Snively, 2019). This is a multi-fluid (6 ions +
 416 electrons), quasi-electrostatic model with its particle continuity consisting of chemical
 417 production/loss and photo/impact ionization. Calculations of local densities, plasma flows,
 418 and temperatures are treated self-consistently and the model includes thermal conduction
 419 heat flux, collisional heating, thermoelectric electron heat flux, and inelastic cooling/heating
 420 from photoelectrons. This is supplemented with Maxwell's equations and, at the time of writing,
 421 includes no displacement current or magnetic induction effects. With this, the system is solved
 422 through enforcing divergence-free currents, curl-free electric fields, and invoking Ohm's law.
 423 **Note: coming this fall: adaptive mesh refinement and neutral coupling!**
 424

425 3.2 Simulation examples

426 Figure 9 shows GEMINI output data with Figure 7C as the plasma flow driver and
 427 the same precipitation data used by example “c5” from Clayton et al. (2021). Unlike previous
 428 figures, this figure/simulation has \mathbf{v}_{bg} put back in. The calculated topside FAC
 429 slice is taken at an altitude of 200 km, but is translated down in this figure to 80 km for
 430 visualization purposes. Similarly, the electron density slice is taken at the center but moved
 431 to the eastern wall. In order to visualize FAC closure, we opt for current flux tubes which
 432 are made possible by the GEMINI enforced condition of $\nabla \cdot \mathbf{j} = 0$ and the use of streamlines
 433 sourced at closed elliptical curves (solid black curves). This enables an intuitive inter-
 434 pretation of auroral current closure by showing where a patch of FAC joins back with
 435 the magnetosphere or where a region of Hall current exits the model space. The dotted
 436 black and blue curves show the projection of the terminating ends of the flux tubes onto
 437 the FAC map. The green flux tube (28.4 kA) represents a stereotypical example of FAC
 438 closure via the Pedersen layer, closing down between 118 - 154 km. The orange tube (31.0
 439 kA) runs underneath it in the Hall layer and shows exchange between a region of Hall
 440 current and Pedersen current up near the bottom of the Pedersen layer. This tube spans
 441 between 87 - 105 km in altitude at its lowest point, and exits the equatorward wall be-
 442 tween 101 - 138 km. The red flux tube (23.9 kA) is, to some extent, a combination of
 443 these two, and has two exit regions. When this tube runs out of upward FAC to close
 444 through in its nearest current sheet, it continuous onto the next upward FAC sheet pole-
 445 ward of it where the remaining 2.5 kA is closed.

446 To show the effects of steps 2 and 3 of section 2.2.2, the output from Figure 9 is
 447 also simulated with the same precipitation maps, but with the replication scaling and
 448 rotating turned off (see Figure 7D-F). Figure 10 divides the topside FAC maps of both
 449 simulations into the three terms from Eq. (1) in order to look at the effects of the plasma
 450 flow shear and precipitation gradients separately. Figure 10D shows sensible results given
 451 a single arc boundary, but panels E and F illustrate an amalgamation of two apparent
 452 arc profiles at the poleward edge of the arc; even though this replication is fully trans-
 453 parent to the secondary boundary, the Pedersen and Hall conductance gradients cause
 454 the secondary boundary to substantiate. In contrast, Figures 10A-C show clean align-
 455 ment between both arc boundaries for all three FAC terms.

456 4 Discussions

457 4.1 Improvements to auroral plasma flow mapping

458 Figure 9 indicates that even for basic examples of auroral arc systems, the mor-
 459 phology of current closure is 3D in nature. The green flux tube depicts a more instinc-
 460 tive (Mallinckrodt, 1985) auroral current closure type using largely Pedersen currents
 461 to close, however, the red flux tube illustrates a less common view of FAC current clo-
 462 sure; not all current from one FAC sheet has to close with its neighbouring sheet. The
 463 section of the sourced FAC furthest equatorward has to “dig” deeper into the Hall layer,
 464 subsequently rotating, in search of another closure path. Secondly, the orange flux tube

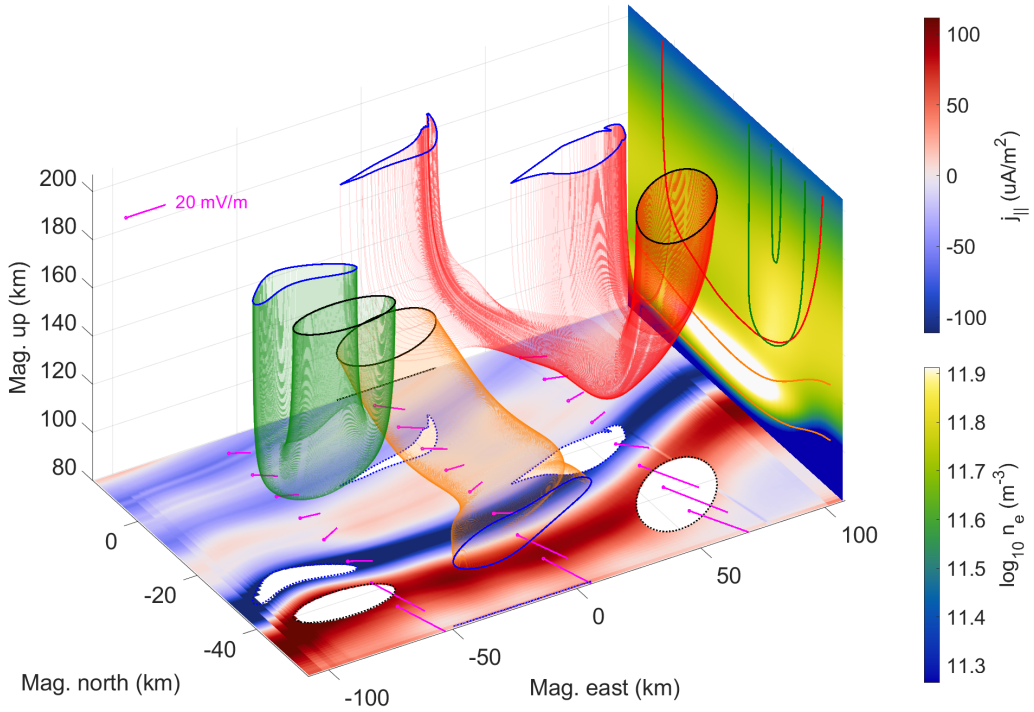


Figure 9. Plasma flow driven GEMINI output with input from the potential in Figure 7C. Current flux tubes are colored for distinction purposes and start/end at solid black/blue curves. The orange flux tube runs in reverse. **East side:** A north-up slice of electron density taken at 0 km east along with flux tube outline projections. **Bottom side:** An east-north slice of FAC (with parallel being down) taken at 200 km altitude along with flux tube start/end curve projections and electric field vectors (magenta). Note that these vectors include the background electric field.

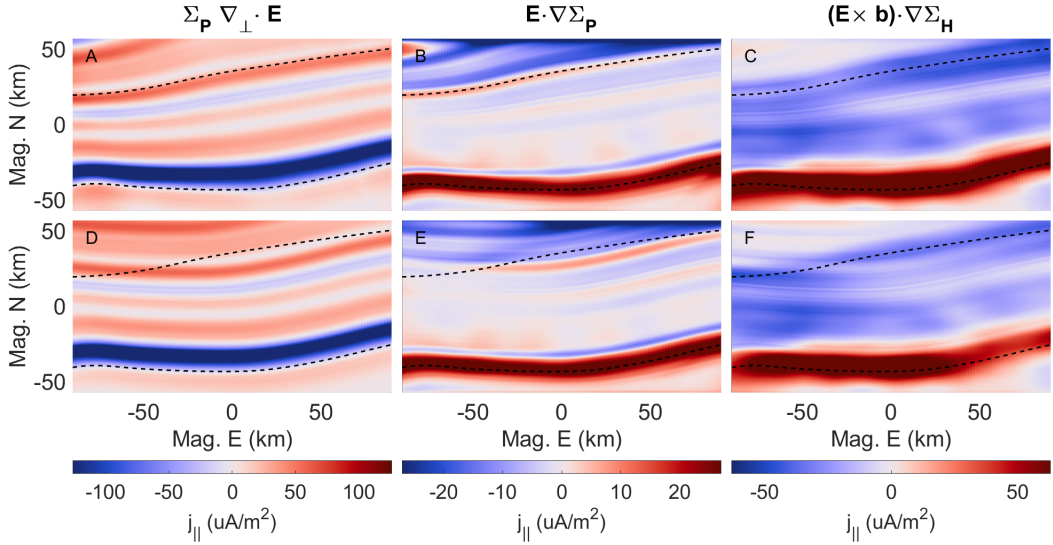


Figure 10. Calculated FAC components from Eq. (1). **A-C:** Terms 1 through 3 respectively split from the FAC map shown in Figure 9 along with arc boundaries (dashed). **D-F:** Same as the top row but with replication scaling and rotating turned off.

465 is mostly Hall current, but includes divergence, i.e. the last term in Eq. (1), which is being
 466 fed by Pedersen currents as the tube descends from regions of higher conductivity
 467 (see the electron density panel). The Pedersen current being used by this closure can no
 468 longer be used to close FACs, which is how diverging Hall currents can indirectly effect
 469 topside F-region currents. Moreover, FAC closure is not restricted to the Pedersen or Hall
 470 layers (90 - 130 km); depending on the perpendicular distance from the FAC sheet in-
 471 flexion line, closure can happen at altitudes as high as 154 km in this instance. From
 472 a current flux conservation standpoint, this is a matter of compromising the lower con-
 473 ductivity at these heights with larger flux tube cross-section.

474 All this 3D structure is attributable to the interplay of the altitude dependent Ped-
 475 ersen and Hall conductivities as a region of current attempts to find the path of least re-
 476 sistance. To better understand electrostatic auroral arc scale science, and the non-passive
 477 role the ionosphere plays in MI coupling, these 3D features require further studies, which
 478 in turn requires 3D auroral simulations and thus this provides the need for continuous,
 479 topside F-region, electrostatic plasma convection maps.

480 We have developed techniques for creating such maps which focus on anisotropic
 481 auroral physical and gradient scale lengths, and discrete sheet-like morphologies. The
 482 reconstruction, replication, and weighted replication methodology all aim to use max-
 483 imal information from imagery derived precipitation maps to get the most intuitive plasma
 484 flow maps possible. This is achieved by the following improvements to work done by (Clayton
 485 et al., 2019):

- 486 1. Opting for imagery derived Pedersen conductance contour lines, in place of en-
 ergy flux gradients, as a more natural choice for copying electric field data.
- 487 2. Using a secondary auroral arc boundary to which the plasma flow data are scaled
 in an attempt to co-locate shorted-out electric fields with enhanced precipitation.
- 488 3. Plasma flow rotation to ensure the zeroth order electric field shock definition of
 auroral arcs.

492 Figure 7 and 10 demonstrate these improvements. These additional measures ensure that
 493 the relative directions between the electric fields and the imagery related gradients are
 494 more intuitive, and they represent the next step toward studying auroral arcs that stray
 495 from their ideal, sheet-like morphologies.

496 4.2 Cautionary remarks

497 The Gaussian smoothing of the plasma flow data (referred to in Section 2.2.2) should
 498 not be arbitrary. Eq. (1) shows that the gradients in the track direction directly affect
 499 the magnitude of the FAC. The resolution of the optical data (often the limiting reso-
 500 lution [A. Mule is improving this](#)) should determine the scale length of the Gaussian fil-
 501 tering of the plasma flow data in such a way that the Pedersen and Hall conductance
 502 gradient terms closely match the diverging electric field term in Eq. (1) in overall peak
 503 magnitudes. For example, Figure 8 shows a precipitation and conductance map that are
 504 of similar gradient scale lengths to that of the resulting plasma flow maps. As a vali-
 505 dation check, the area integral of the model calculated FAC map over the region of inter-
 506 est should approximately vanish. In case both Pedersen and Hall conductances are avail-
 507 able, this check can also be performed prior to simulating.

508 As a second cautionary reminder, the replicated plasma flow interpolation (see Sec-
 509 tion 2.2.3) needs to be done using cubic or cubic spline methods to ensure a continuity
 510 of C^1 or higher. Using linear interpolation results in strong rippling of simulated FAC
 511 because of discontinuous first derivatives of the electric field.

512 5 Conclusions and future work

513 Measurements of auroral arc systems can be sparse, heterogeneous, and largely dis-
 514 tributed, while ionospheric models generally require continuous topside boundary con-
 515 ditions. We have circumvented this limitation by using extensive information from multi-
 516 spectral, all-sky imagery. We have outlined three empirical methods for creating elec-
 517 trostatic, continuous, topside F-region convection boundary conditions that focus on typ-
 518 ical sheet-like discrete auroral arc structures. The main takeaways are as follows:

- 519 1. Even for the most basic auroral arc systems, a 2D (latitude-altitude) description
 520 is insufficient and hides the 3D nature of current closure.
- 521 2. When extrapolating F-region plasma flow data surrounding auroral arcs, it is im-
 522 portant to scale the data in a way that co-locates the associated shorted out elec-
 523 tric fields with the region of enhanced conductance.
- 524 3. Similarly, it is important to rotate the plasma flow data to avoid introducing un-
 525 intuitive angles between the ionospheric electric field and the conductance gradi-
 526 ents.

527 5.1 Future work

528 This work will be used to address the question of “what self-consistency constraints
 529 exist in creating a geophysically coherent set of F-region, quasistatic auroral system drivers?”.
 530 Finding a set of electrostatic auroral conductances, convection flow, and FAC maps that
 531 are physical and self-consistent is fully determined by Eq. (1). Finding a set that appears
 532 in nature, on Earth, and is likely, requires more intuition and understanding of the in-
 533 terplay between these three ingredients. The techniques outlined in this paper will be
 534 used to develop a sub-catalog of data-driven 3D simulations mainly provided by events
 535 from the *Swarm-over-Poker-2023* campaign (and perhaps also use convection flow data
 536 provided by EISCAT 3D (Stamm et al., 2021) in the future). Additionally, the replica-
 537 tion technique can possibly be merged with Lompe (Laundal et al., 2022) to provide even
 538 more self-consistency. [expand on this](#)

539 As a side note, a possible improvement to the replication technique would be to
 540 have each individual plasma flow data point from each track follow the conductance con-
 541 tour line it sits on, while still rotating accordingly, creating essentially a continuous set
 542 of arc boundaries. This idea, however, has not yet been explored at the time of writing.

543 After gathering a sub-catalog of data driven simulations, they will be idealized to
 544 retain only the simplest structures (peak precipitation flux, flow shear, arc width, etc.)
 545 where the resulting data-*inspired* simulations can be defined by a manageable number
 546 of parameters. From there, this parameter space will be strategically explored, gradu-
 547 ally straying from their ideal, sheet-like structure, which will create the remainder of the
 548 simulation catalog, where understanding the physical mechanisms connecting these var-
 549 ious parameters will aid in studying the data-driven simulations. This catalog and its
 550 supplementary setup, driving, and analysis infrastructure will be made publicly avail-
 551 able in a way that makes it easily expandable. This will all be covered in future paper,
 552 so stay tuned.

553 Open Research Section

554 The ARCS OSSE used in this work and the 3D simulation data are available at
 555 <https://rcweb.dartmouth.edu/LynchK/Gemini3D/>. The Isinglass data and imagery
 556 inversions are at <https://rcweb.dartmouth.edu/LynchK/pubdata/>. Poker Flat DASC
 557 data are at <http://optics.gi.alaska.edu/optics/archive>. AMISR data are avail-
 558 able at <https://data.amisr.com/database/>. Swarm TII data are available at <https://>

559 `swarm-diss.eo.esa.int/` and GEMINI source code is available at <https://github.com/gemini3d>.
 560

561 Acknowledgments

562 We thank NASA for funding Jules van Irsel from grant 80NSSC23K1622 through the
 563 FINESST program and Dartmouth College for providing internal funding for Phase A
 564 of the Auroral Reconstruction CubeSwarm proposal (ARCS) from which a lot of this re-
 565 search stems, and we acknowledge NASA grant 80GSFC21C0009 for the ARCS MIDEX
 566 CSR funding. We are grateful for the data providers from the Isinglass rocket team and
 567 we acknowledge Isinglass LCAS support from NASA grant NNX14AH07G. [DASC data](#)
 568 [url + grants](#) The Poker Flat Incoherent Scatter Radar is operated by the SRI Interna-
 569 tional for the National Science Foundation as part of the AMISR program through co-
 570 operative agreement AGS-1840962. This work uses Level 1B data from the Thermal Ion
 571 Imagers made possible by the European Space Agency's Swarm Data, Innovation, and
 572 Science Cluster. We thank NASA for providing funding for the GEMINI model devel-
 573 opment from grant 80NSSC24K0126. 3D simulations supporting this work were provided
 574 by the Discovery cluster at Dartmouth Research Computing and the NASA High-End
 575 Computing (HEC) Program through the NASA Advanced Supercomputing (NAS) Di-
 576 vision at Ames Research Center. We would like to thank Michael Hirsch (B.U.), Terry
 577 Kovacs, and John Griffin (Dartmouth College) for invaluable GEMINI and computational
 578 technical support and we also like to thank Meghan Burleigh for her invaluable input
 579 in reviewing this manuscript. Lastly we thank Don Hampton and Leslie Lamarche, along
 580 with NSF grant 2329979, for providing support for the 2023 *Swarm-over-Poker* campaign.

581 References

- 582 Ahlfors, L. V. (1953). Complex analysis: an introduction to the theory of analytic
 583 functions of one complex variable. *New York, London, 177.*
- 584 Amm, O. (1997). Ionospheric elementary current systems in spherical coordinates
 585 and their application. *Journal of geomagnetism and geoelectricity*, 49(7), 947-
 586 955. doi: 10.5636/jgg.49.947
- 587 Archer, W. E., Knudsen, D. J., Burchill, J. K., Jackel, B., Donovan, E., Connors,
 588 M., & Juusola, L. (2017). Birkeland current boundary flows. *Journal of Geo-
 589 physical Research: Space Physics*, 122(4), 4617-4627. Retrieved from <https://agupubs.onlinelibrary.wiley.com/doi/abs/10.1002/2016JA023789> doi:
 590 <https://doi.org/10.1002/2016JA023789>
- 591 Bristow, W. A., Hampton, D. L., & Otto, A. (2016). High-spatial-resolution velocity
 592 measurements derived using Local Divergence-Free Fitting of SuperDARN
 593 observations. *Journal of Geophysical Research: Space Physics*, 121(2), 1349-
 594 1361. Retrieved from <https://agupubs.onlinelibrary.wiley.com/doi/abs/10.1002/2015JA021862> doi: <https://doi.org/10.1002/2015JA021862>
- 595 Clayton, R., Burleigh, M., Lynch, K. A., Zettergren, M., Evans, T., Grubbs, G., ...
 596 Varney, R. (2021). Examining the auroral ionosphere in three dimensions using
 597 reconstructed 2D maps of auroral data to drive the 3D GEMINI model. *Jour-
 598 nal of Geophysical Research: Space Physics*, 126(11). Retrieved from <https://agupubs.onlinelibrary.wiley.com/doi/abs/10.1029/2021JA029749> doi:
 599 <https://doi.org/10.1029/2021JA029749>
- 600 Clayton, R., Lynch, K., Zettergren, M., Burleigh, M., Conde, M., Grubbs, G., ...
 601 Varney, R. (2019). Two-dimensional maps of in situ ionospheric plasma
 602 flow data near auroral arcs using auroral imagery. *Journal of Geophysi-
 603 cal Research: Space Physics*, 124(4), 3036-3056. Retrieved from <https://agupubs.onlinelibrary.wiley.com/doi/abs/10.1029/2018JA026440> doi:
 604 <https://doi.org/10.1029/2018JA026440>
- 605 Cowley, S. W. H. (2000). Magnetosphere-ionosphere interactions: A tutorial review.

- 610 *Magnetospheric Current Systems, Geophysical Monograph Series, 118*, 91-106.
- 611 Enengl, F., Kotova, D., Jin, Y., Clausen, L. B. N., & Miloch, W. J. (2023). Ionospheric plasma structuring in relation to auroral particle precipitation. *J. Space Weather Space Clim.*, 13. Retrieved from <https://doi.org/10.1051/swsc/2022038> doi: 10.1051/swsc/2022038
- 612 Erlandson, R., Lynch, K. A., Samara, M., Anderson, B., Bortnik, J., Burleigh, M., ...
613 Zou, S. (2024). *Auroral Reconstruction CubeSwarm (ARCS)*. (Manuscript in
614 Preperation)
- 615 Fang, X., Randall, C. E., Lummerzheim, D., Solomon, S. C., Mills, M. J., Marsh,
616 D. R., ... Lu, G. (2008). Electron impact ionization: A new parameterization
617 for 100 ev to 1 mev electrons. *Journal of Geophysical Research: Space Physics*,
618 113(A9). Retrieved from <https://agupubs.onlinelibrary.wiley.com/doi/abs/10.1029/2008JA013384> doi: <https://doi.org/10.1029/2008JA013384>
- 619 Fang, X., Randall, C. E., Lummerzheim, D., Wang, W., Lu, G., Solomon, S. C., &
620 Frahm, R. A. (2010). Parameterization of monoenergetic electron impact
621 ionization. *Geophysical Research Letters*, 37(22). Retrieved from <https://agupubs.onlinelibrary.wiley.com/doi/abs/10.1029/2010GL045406> doi:
622 <https://doi.org/10.1029/2010GL045406>
- 623 Fujii, R., Amm, O., Vanhamäki, H., Yoshikawa, A., & Ieda, A. (2012, 11).
624 An application of the finite length cowling channel model to auroral arcs
625 with longitudinal variations. *Journal of Geophysical Research*, 117. doi:
626 <https://doi.org/10.1029/2012JA017953>
- 627 Fujii, R., Amm, O., Yoshikawa, A., Ieda, A., & Vanhamäki, H. (2011). Reformulation and energy flow of the Cowling channel. *Journal of Geophysical Research: Space Physics*, 116(A2). Retrieved from <https://agupubs.onlinelibrary.wiley.com/doi/abs/10.1029/2010JA015989> doi:
628 <https://doi.org/10.1029/2010JA015989>
- 629 Grubbs II, G., Michell, R., Samara, M., Hampton, D., Hecht, J., Solomon, S., &
630 Jahn, J. (2018). A comparative study of spectral auroral intensity predictions from multiple electron transport models. *Journal of Geophysical Research: Space Physics*, 123(1), 993-1005. Retrieved from <https://agupubs.onlinelibrary.wiley.com/doi/abs/10.1002/2017JA025026> doi:
631 <https://doi.org/10.1002/2017JA025026>
- 632 Grubbs II, G., Michell, R., Samara, M., Hampton, D., & Jahn, J. (2018). Predicting
633 electron population characteristics in 2-d using multispectral ground-based
634 imaging. *Geophysical Research Letters*, 45(1), 15-20. Retrieved from <https://agupubs.onlinelibrary.wiley.com/doi/abs/10.1002/2017GL075873> doi:
635 <https://doi.org/10.1002/2017GL075873>
- 636 Heinselman, C. J., & Nicolls, M. J. (2008). A Bayesian approach to electric field
637 and E-region neutral wind estimation with the Poker Flat Advanced Modular
638 Incoherent Scatter Radar. *Radio Science*, 43(5). Retrieved from <https://agupubs.onlinelibrary.wiley.com/doi/abs/10.1029/2007RS003805> doi:
639 <https://doi.org/10.1029/2007RS003805>
- 640 Kaepller, S., Markowski, D. G., Pepper, A. M., Troyer, R., Jaynes, A. N., Varney,
641 R. H., & Hampton, D. (2023, 9). Data-driven empirical conductance relations during auroral precipitation using incoherent scatter radar
642 and all sky imagers. *Journal of Geophysical Research: Space Physics*. doi:
643 <https://doi.org/10.1029/2023JA031764>
- 644 Kamide, Y., Richmond, A. D., & Matsushita, S. (1981). Estimation of ionospheric
645 electric fields, ionospheric currents, and field-aligned currents from ground
646 magnetic records. *Journal of Geophysical Research: Space Physics*, 86(A2),
647 801-813. Retrieved from <https://agupubs.onlinelibrary.wiley.com/doi/abs/10.1029/JA086iA02p00801> doi: <https://doi.org/10.1029/JA086iA02p00801>
- 648 Kelley, M. C. (2009). *The Earth's ionosphere: plasma physics and electrodynamics*

- (2nd ed.). Amsterdam, Netherlands: Academic Press.
- Kelly, J., & Heinselman, C. (2009). Initial results from Poker Flat Incoherent Scatter Radar (PFISR). *Journal of Atmospheric and Solar-Terrestrial Physics*, 71(6), 635. Retrieved from <https://www.sciencedirect.com/science/article/pii/S1364682609000121> (Advances in high latitude upper atmospheric science with the Poker Flat Incoherent Scatter Radar (PFISR)) doi: <https://doi.org/10.1016/j.jastp.2009.01.009>
- Khazanov, G. V., Robinson, R. M., Zesta, E., Sibeck, D. G., Chu, M., & Grubbs, G. A. (2018). Impact of precipitating electrons and magnetosphere-ionosphere coupling processes on ionospheric conductance. *Space Weather*, 16(7), 829-837. Retrieved from <https://agupubs.onlinelibrary.wiley.com/doi/abs/10.1029/2018SW001837> doi: <https://doi.org/10.1029/2018SW001837>
- Knudsen, D. J., Burchill, J. K., Buchert, S. C., Eriksson, A. I., Gill, R., Wahlund, J.-E., ... Moffat, B. (2017). Thermal ion imagers and langmuir probes in the Swarm electric field instruments. *Journal of Geophysical Research: Space Physics*, 122(2), 2655-2673. Retrieved from <https://agupubs.onlinelibrary.wiley.com/doi/abs/10.1002/2016JA022571> doi: <https://doi.org/10.1002/2016JA022571>
- Laundal, K. M., Reistad, J. P., Hatch, S. M., Madelaire, M., Walker, S., Hovland, A. Ø., ... Sorathia, K. A. (2022). Local mapping of polar ionospheric electrodynamics. *Journal of Geophysical Research: Space Physics*, 127(5). Retrieved from <https://agupubs.onlinelibrary.wiley.com/doi/abs/10.1029/2022JA030356> doi: <https://doi.org/10.1029/2022JA030356>
- Lotko, W. (2004). Inductive magnetosphere-ionosphere coupling. *Journal of Atmospheric and Solar-Terrestrial Physics*, 66(15), 1443-1456. Retrieved from <https://www.sciencedirect.com/science/article/pii/S1364682604001518> doi: <https://doi.org/10.1016/j.jastp.2004.03.027>
- Lynch, K. A., Erlandson, R., Samara, M., Anderson, B., Bortnik, J., Burleigh, M., ... Zou, S. (2024). *Auroral Reconstruction CubeSwarm (ARCS)*. (Manuscript in Preperation)
- Lynch, K. A., McManus, E., Gutow, J., Burleigh, M., & Zettergren, M. (2022). An ionospheric conductance gradient driver for subauroral picket fence visible signatures near STEVE events. *Journal of Geophysical Research: Space Physics*, 127(12). Retrieved from <https://agupubs.onlinelibrary.wiley.com/doi/abs/10.1029/2022JA030863> doi: <https://doi.org/10.1029/2022JA030863>
- Mallinckrodt, A. J. (1985). A numerical simulation of auroral ionospheric electrodynamics. *Journal of Geophysical Research: Space Physics*, 90(A1), 409-417. Retrieved from <https://agupubs.onlinelibrary.wiley.com/doi/abs/10.1029/JA090iA01p00409> doi: <https://doi.org/10.1029/JA090iA01p00409>
- Marghitu, O. (2012). Auroral arc electrodynamics: Review and outlook. *Relationship between auroral phenomenology and magnetospheric processes: Earth and other planets, Geophysical Monograph Series*, 197, 143-158.
- Nicolls, M. J., Cosgrove, R., & Bahcivan, H. (2014). Estimating the vector electric field using monostatic, multibeam incoherent scatter radar measurements. *Radio Science*, 49(11), 1124-1139. Retrieved from <https://agupubs.onlinelibrary.wiley.com/doi/abs/10.1002/2014RS005519> doi: <https://doi.org/10.1002/2014RS005519>
- Nicolls, M. J., & Heinselman, C. J. (2007). Three-dimensional measurements of traveling ionospheric disturbances with the Poker Flat Incoherent Scatter Radar. *Geophysical Research Letters*, 34(21). Retrieved from <https://agupubs.onlinelibrary.wiley.com/doi/abs/10.1029/2007GL031506> doi: <https://doi.org/10.1029/2007GL031506>
- Richmond, A. D., & Kamide, Y. (1988). Mapping electrodynamic features of the high-latitude ionosphere from localized observations: Technique. *Journal of Geophysical Research: Space Physics*, 93(A6), 5741-5759. Retrieved

- 720 from <https://agupubs.onlinelibrary.wiley.com/doi/abs/10.1029/JA093iA06p05741> doi: <https://doi.org/10.1029/JA093iA06p05741>
- 721 Robinson, R. M., Vondrak, R. R., Miller, K., Dabbs, T., & Hardy, D. (1987). On
 722 calculating ionospheric conductances from the flux and energy of precipitating
 723 electrons. *Journal of Geophysical Research: Space Physics*, 92(A3), 2565-
 724 2569. Retrieved from <https://agupubs.onlinelibrary.wiley.com/doi/abs/10.1029/JA092iA03p02565> doi: <https://doi.org/10.1029/JA092iA03p02565>
- 725 Ruohoniemi, J. M., Greenwald, R. A., Baker, K. B., Villain, J. P., Hanuise, C., &
 726 Kelly, J. (1989). Mapping high-latitude plasma convection with coherent HF
 727 radars. *Journal of Geophysical Research: Space Physics*, 94(A10), 13463-13477.
 728 Retrieved from <https://agupubs.onlinelibrary.wiley.com/doi/abs/10.1029/JA094iA10p13463> doi: <https://doi.org/10.1029/JA094iA10p13463>
- 729 Seyler, C. E. (1990). A mathematical model of the structure and evolution
 730 of small-scale discrete auroral arcs. *Journal of Geophysical Research: Space Physics*, 95(A10), 17199-17215. Retrieved from <https://agupubs.onlinelibrary.wiley.com/doi/abs/10.1029/JA095iA10p17199> doi: <https://doi.org/10.1029/JA095iA10p17199>
- 731 Sobel, I. (2014, 02). An isotropic 3x3 image gradient operator. *Presentation at Stanford A.I. Project 1968*.
- 732 Solomon, S. C. (2017). Global modeling of thermospheric airglow in the far ultraviolet. *Journal of Geophysical Research: Space Physics*, 122(7), 7834-7848. Retrieved from <https://agupubs.onlinelibrary.wiley.com/doi/abs/10.1002/2017JA024314> doi: <https://doi.org/10.1002/2017JA024314>
- 733 Stamm, J., Vierinen, J., Urco, J. M., Gustavsson, B., & Chau, J. L. (2021). Radar
 734 imaging with EISCAT 3D. *Annales Geophysicae*, 39(1), 119-134. Retrieved
 735 from <https://angeo.copernicus.org/articles/39/119/2021/> doi:
 736 <https://doi.org/10.5194/angeo-39-119-2021>
- 737 Wang, X., Cai, L., Aikio, A., Vanhamäki, H., Virtanen, I., Zhang, Y., ... Liu,
 738 S. (2024). Ionospheric conductances due to electron and ion precipitations: A comparison between EISCAT and DMSP estimates. *Journal of Geophysical Research: Space Physics*, 129(2). Retrieved from <https://agupubs.onlinelibrary.wiley.com/doi/abs/10.1029/2023JA032354> doi: <https://doi.org/10.1029/2023JA032354>
- 739 Wolf, R. A. (1975, Mar 01). Ionosphere-magnetosphere coupling. *Space Science Reviews*, 17(2), 537-562. Retrieved from <https://doi.org/10.1007/BF00718584> doi: [10.1007/BF00718584](https://doi.org/10.1007/BF00718584)
- 740 Yano, Y., & Ebihara, Y. (2021). Three-dimensional closure of field-aligned currents in the polar ionosphere. *Journal of Geophysical Research: Space Physics*, 126(9). Retrieved from <https://agupubs.onlinelibrary.wiley.com/doi/abs/10.1029/2021JA029421> doi: <https://doi.org/10.1029/2021JA029421>
- 741 Zettergren, M., & Snively, J. (2019). Latitude and longitude dependence of ionospheric TEC and magnetic perturbations from infrasonic-acoustic waves generated by strong seismic events. *Geophysical Research Letters*, 46(3), 1132-1140. doi: [10.1029/2018GL081569](https://doi.org/10.1029/2018GL081569)
- 742 Zettergren, M. D., & Semeter, J. L. (2012). Ionospheric plasma transport and loss in auroral downward current regions. *Journal of Geophysical Research: Space Physics*, 117(A6). Retrieved from <https://agupubs.onlinelibrary.wiley.com/doi/abs/10.1029/2012JA017637> doi: <https://doi.org/10.1029/2012JA017637>